Nanoscale

PAPER

View Article Online
View Journal | View Issue

Cite this: *Nanoscale*, 2020, **12**, 20699

Minimizing two-dimensional $Ti_3C_2T_x$ MXene nanosheet loading in carbon-free silicon anodes†

Kasturi T. Sarang,[a] Xiaofei Zhao,[a] Dustin Holta,[b] Miladin Radovic,[b] Micah J. Green, [a,b] Eun-Suok Oh *[c] and Jodie L. Lutkenhaus *[a,b]

Received 21st August 2020,
Accepted 23rd September 2020

DOI: 10.1039/d0nr06086k

rsc.li/nanoscale

Silicon anodes are promising for high energy batteries because of their excellent theoretical gravimetric capacity (3579 mA h g^{-1}). However, silicon's large volume expansion and poor conductivity hinder its practical application; thus, binders and conductive additives are added, effectively diluting the active silicon material. To address this issue, reports of 2D MXene nanosheets have emerged as additives for silicon anodes, but many of these reports use high MXene compositions of 22–66 wt%, still presenting the issue of diluting the active silicon material. Herein, this report examines the question of what minimal amount of MXene nanosheets is required to act as an effective additive while maximizing *total* silicon anode capacity. A minimal amount of only 4 wt% MXenes (with 16 wt% sodium alginate and no carbon added) yielded silicon anodes with a capacity of 900 mA h g_{Si}^{-1} or 720 mA h g_{total}^{-1} at the 200th cycle at 0.5 C-rate. Further, this approach yielded the highest specific energy on a *total* electrode mass basis (3100 W h kg_{total}^{-1}) as comapared to other silicon-MXene constructs (~115–2000 Wh kg_{total}^{-1}) at a corresponding specific power. The stable electrode performance even with a minimal MXene content is attributed to several factors: (1) highly uniform silicon electrodes due to the dispersibility of MXenes in water, (2) the high MXene aspect ratio that enables improved electrical connections, and (3) hydrogen bonding among MXenes, sodium alginate, and silicon particles. All together, a much higher silicon loading (80 wt%) is attained with a lower MXene loading, which then maximizes the capacity of the entire electrode.

Introduction

Lithium-ion batteries have become important power sources for small electronics such as mobile phones and laptops.[1,2] However, current lithium-ion batteries (LIBs) still require improvements in energy density for electric vehicles and large-scale wind/solar power grids.[3,4] In order to address these issues, researchers are working on improving the performance of the battery's electrodes.[5,6] Conventionally, graphite is used as an anode material in LIBs; however, it has a low theoretical capacity of 350 mA h g^{-1}.[6] On the other hand, silicon anodes have a very high theoretical capacity of 3579 mA h g^{-1} because they can store up to 3.75 Li^+ ions per silicon atom.[7,8] Further, silicon has a low discharge potential (~0.3 V *vs.* Li/Li^+), and it is abundantly available in nature.[3,9] In spite of these advantages, silicon faces several major drawbacks. Silicon undergoes 300% volumetric expansion during lithiation which builds up internal stresses and causes pulverization. Silicon nanoparticles (diameter ≤ 150 nm) alleviate pulverization,[7,10] but other issues affiliated with volumetric expansion still persist (*e.g.* delamination from the current collector,[1] unstable build-up of the solid electrolyte interphase (SEI),[11,12] loss of electrical percolation[13]). This manifests as capacity fade and poor coulombic efficiency.

To address the aforementioned issues, binders and conductive additives – over 30 wt% – are commonly added to silicon anodes.[14] These additives improve the overall function of the electrode, but they dilute the active silicon material. The challenge we explore here is the minimization of additives while preserving function and maximizing the amount of active silicon.

Several water-based polymeric binders have been studied for silicon anodes:[15,16] polyacrylic acid (PAA),[17,18] carboxymethyl cellulose (CMC),[19] alginate (Alg),[20] and polydopamine (PD).[21] The general observation is that hydrogen bonding interactions between the binder and the hydroxyl (–OH) groups on the silicon surface bind the electrode together.

[a]*Artie McFerrin Department of Chemical Engineering, Texas A&M University, College Station, Texas 77843, USA. E-mail: jodie.lutkenhaus@tamu.edu*
[b]*Department of Material Science & Engineering, Texas A&M University, College Station, TX 77843, USA*
[c]*School of Chemical Engineering, University of Ulsan, Ulsan 44611, South Korea. E-mail: esoh1@ulsan.ac.kr*

†Electronic supplementary information (ESI) available. See DOI: 10.1039/d0nr06086k

Another important electrode component is the conductive additive. Super P carbon black (CB) is the most commonly used conductive additive in silicon anodes.[22] Researchers have also explored several carbonaceous materials such as graphene,[23–25] carbon nanotubes,[22,26] and carbon nanofibers.[27] However, CB and other carbonaceous materials are hydrophobic, which complicates water-based processing.

Recently, MXenes, have been explored as conducting additives in silicon anodes. MXenes are 2D nanosheets prepared by selectively extracting the "A" element from their corresponding three-dimensional MAX phases, where M represents an early transition metal, A is a group 13–16 element, and X is either a C and/or N.[28,29] The most commonly examined MXene is $Ti_3C_2T_x$, which has a high conductivity (4600 S cm^{-1}), excellent Li^+-ion diffusion (~10^{-10}–10^{-9} cm^2 s^{-1}), and good mechanical properties.[30,31] $Ti_3C_2T_x$ nanosheets are also redox active in the potential window of 0–3 V *vs.* Li/Li^+.[30,32] MXenes are hydrophilic due to the presence of terminal hydroxyl (–OH) groups on their surface. These properties have been utilized to make water-based polymer-MXenes composites by simple mixing processes.[33–35] Here, we represent $Ti_3C_2T_x$ nanosheets as "MX" for simplicity.

The literature shows a theme in that huge quantities of MXenes and/or additional additives are needed to prepare functional silicon anodes, effectively lowering the active material (silicon) loading and the total electrode capacity. The capacity values listed in this paragraph are the ones reported in long-term battery cycling tests. Kong *et al.*[36] made silicon electrodes with 66 wt% of MXenes along with additional binder and CB. The high additive content lowered the silicon amount to 13 wt%, which then lowered the total electrode capacity (24.4 mA h g_{total}^{-1} at C-rate of ~0.05 C). On the other hand, Zhu *et al.*[37] made electrodes with 43 wt% of silicon by adding 22 wt% MXenes and additional additives (binder and CB). These electrodes demonstrated a total capacity 740 mA h g_{total}^{-1} at a C-rate of ~0.1 C. Lastly, Zhang *et al.*[13] used 30 wt% MXenes (Si content = 70 wt%) to make silicon electrodes without adding any binder or additional carbon additives, and they demonstrated a total capacity of 1050 mA h g_{total}^{-1} at a C-rate of ~0.35 C.

There are a few reports that have utilized different approaches to minimize the dead weight (which includes binder and carbon additives) in silicon anodes.[38–41] We proposed that utilization of MXenes along with a suitable binder (without any additional carbon additives) would reduce this dead weight and ultimately increase the silicon content in the electrode.

Here, we explored the minimization of MXene content in the pursuit of maximal silicon loading, while developing a fundamental understanding how MXenes behave in the electrode. Sodium alginate (Alg) was also added to the silicon electrodes because its –OH groups hydrogen bond with silicon[20] and MXenes. To evaluate the battery performance, we used cyclic voltammetry to study the lithiation kinetics of the silicon anode, galvanostatic charge/discharge cycling to study the stability of the silicon electrode, and electrochemical impedance spectroscopy to determine the electrode impedance. We utilized scanning electron microscopy (SEM) along with energy dispersive X-ray spectroscopy (EDS) to observe the morphologies of electrodes. We also performed X-ray photo electron spectroscopy to characterize the SEI formed after battery cycling. By using MXenes, we increased the Si content to 80 wt% and eliminated CB to yield a comparatively high capacity for silicon/MXene anodes.

Materials and methods

Materials

Silicon nanoparticles (98+% purity, 50–70 nm size, 80–120 m^2 g^{-1} surface area) were acquired from US-research nanomaterials. Sodium alginate (Alg, 15–25 cP, 1% in H_2O), 1 M lithium hexafluorophosphate ($LiPF_6$) in ethylene carbonate (EC) : diethyl carbonate (DEC) (1 : 1) v/v, hydrochloric acid (HCl, ACS reagent 37% w/w), dimethyl sulfoxide (DMSO, ReagentPlus, >99.5%) were acquired from Sigma Aldrich. Lithium foil (0.75 mm thick × 19 mm wide), lithium fluoride (LiF, 98+% purity), fluoroethylene carbonate (FEC), titanium (Ti, 44 μm average particle size, 99.5% purity), aluminum (Al, 44 μm average particle size, 99.5% purity), and titanium carbide (TiC) (2–3 μm average particle size, 99.5% purity) were purchased from Alfa Aesar. Super P carbon black (0.04 μm particle size, 62 m^2 g^{-1} surface area), copper foil (length × width × thickness = 170 m × 280 mm × 9 μm) was purchased from MTI corporation. Polypropylene separator (19 mm diameter × 0.025 mm thick) was purchased from Celgard. Poly(vinyldifluoride) (PVDF) filtration unit with pore size of 0.22 μm was purchased from Milipore (Millipore® SCGVU10RE Stericup™ GV).

MXene synthesis and preparation

MXene synthesis was adopted from literature[42] and is detailed in the ESI.† In brief, the $Ti_3C_2T_x$ MXene layers were obtained by lithium fluoride + hydrochloric acid etching and DMSO delamination. X-ray diffraction (XRD) analysis (Bruker D8 powder X-ray diffractometer) and X-ray photo electron spectroscopy (XPS) (Omicron X-ray photoelectron spectrometer) confirmed the successful synthesis nanosheets (Fig. S1†). After synthesis, the MXenes were freeze dried to form a powder and then stored under vacuum at room temperature to minimize their oxidation. The morphology of the delaminated MXene nanosheets was characterized using scanning electron microscopy (SEM), as shown in Fig. 1a. From atomic force microscopy (AFM, Fig. S2†), the lateral nanosheet size was approximately 1 μm.

To prepare the conductive binder, freeze-dried MXenes were added to sodium alginate solution (1 wt% solution in water) and the mixture was bath-sonicated for one minute to form a homogenous dispersion as shown in Fig. S3a.† Two different Alg/MXene ratios were studied; Alg (90%) + MX (10%) and Alg (80%) + MX (20%).

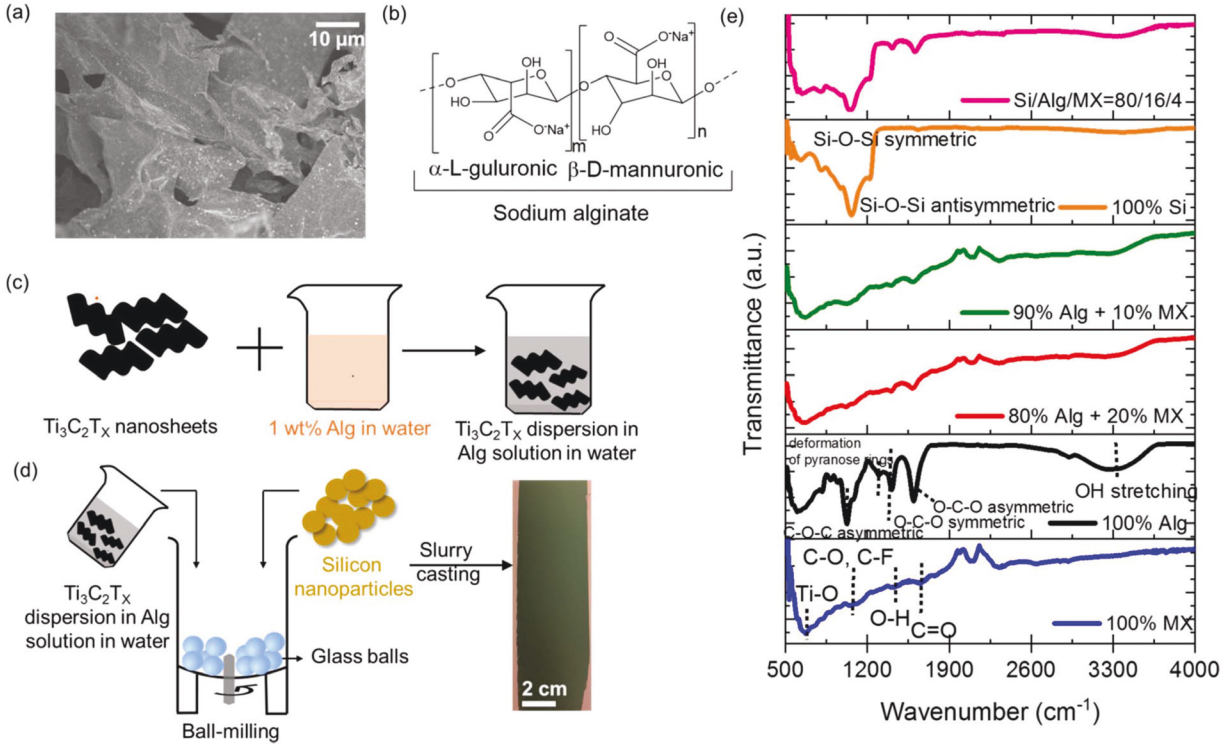

Fig. 1 (a) Scanning electron microscopy (SEM) image of $Ti_3C_2T_x$ nanosheets, (b) schematic of sodium alginate (Alg), (c) schematic of a MXene dispersion in aqueous Alg solution, (d) schematic of electrode fabrication process by slurry casting method, and (e) FTIR spectra of MXenes, Alg, 90 wt% Alg + 10 wt% MX, 80 wt% Alg + 20 wt% MX, silicon nanoparticles, and Si/Alg/MX = 80/16/4 wt% electrode.

Silicon anode preparation

To synthesize silicon electrodes using the prepared composite binder, silicon nanoparticles and the composite binder with a mass ratio of Si : conductive binder = 80 : 20 were ball milled together in water to form a homogenous slurry. Thus, two different slurries were synthesized: Si/Alg/MX = 80/18/2 and 80/16/4 (by mass). The former resulted from the 90 wt% Alg + 10 wt% MXene composite binder, and the latter resulted from the 80 wt% Alg + 20 wt% MXene composite binder. The slurry was doctor-bladed on copper foil using an automatic film applicator (Elcometer 4340 Automatic applicator) and the resulting film thickness after drying was around 8–10 μm. The electrodes were then dried at room temperature for 3–4 h and then under vacuum at room temperature for 2 days. After drying, 16 mm electrodes were punched. The active material loading was kept constant around 0.70 ± 0.05 mg cm^{-2}. For control experiments, two set of electrodes were prepared: Si/Alg = 80/20 and Si/Alg/CB = 80/16/4. These compositions were chosen to keep the ratio of active material to inactive material constant.

Four-point probe characterization

Four-point probe (powered by Keithley 2000, 6221 and two 6514) was used to determine the electronic conductivity. Four dispersions were prepared: 90 wt% Alg + 10 wt% MXenes or CB, 80 wt% Alg + 20 wt% MXenes or CB. These were drop-cast onto glass slides (3 cm × 3 cm) and dried in vacuum for 2 days.

Fourier transform infrared spectroscopy characterization

Attenuated total reflection-Fourier transform infrared (ATR-FTIR) spectra were recorded using an IR Prestige 21 system (Shimadzu Corp.) using IRsolution v. 1.40 software. The solutions/dispersions used included MXenes (1 mg ml^{-1}), Alg (1 mg ml^{-1}), 90 wt% Alg (1 mg ml^{-1}) + 10 wt% MXenes (1 mg ml^{-1}), and 80 wt% Alg (1 mg ml^{-1}) + 20 wt% MXenes (1 mg ml^{-1}). These samples were prepared by drop-casting onto Cu foil (12 mm diameter), followed by drying in vacuum for 2 days. To perform ATR-FTIR spectroscopy on Si/Alg/MX = 80/16/4 composition, 12 mm diameter discs were punched from the slurry-cast Si/Alg/MX electrode. Silicon nanoparticles were characterized in its powder form.

Scanning electron microscopy (SEM) characterization

SEM was carried out on JEOL JSM SEM equipment with an accelerating voltage of 5 kV and a working distance of 15 mm. SEM was performed on fresh and cycled (50 cycles) electrodes. For the cycled electrodes, the two-electrode TOMCell was disassembled in the glovebox, and the electrodes were washed with dichloromethane to remove the residual salt. These electrodes were then dried in a glovebox for 2–3 days and then in vacuum oven at room temperature for 3 days.

Electrochemical characterization

For electrochemical characterization, two-electrode TOMCells were assembled inside an argon-filled glovebox (MBraun

Labstar). 16 mm punched electrodes were used as working electrodes and lithium metal foil (16 mm) was employed as the counter and reference electrode. Two Celgard polypropylene discs (19 mm diameter, thickness) were used as separators. 1 M $LiPF_6$ in EC : DEC with 10 wt% FEC was used as the electrolyte. Galvanostatic charge–discharge cycling, rate capability, and cyclic voltammetry were performed using an Arbin Instrument (HPT-100 mA). The voltage range was 0.01 V to 1 V *vs.* Li/Li^+, and the charge–discharge currents were calculated based on the theoretical capacity of silicon (3579 mA h g^{-1}). For galvanostatic cycling, the electrodes were cycled in constant current (CC) – constant voltage (CV) mode for the first five cycles to condition the electrode. In the CC–CV mode, electrodes were first lithiated at 0.1 C until the potential reached 0.01 V (CC mode) and then the potential was held constant at 0.01 V until the current had decayed to 0.01 C. Electrochemical impedance spectroscopy (EIS) was performed on fresh and on cycled electrodes using a Gamry Potentiostat/Galvanostat (Gamry Interface 1000, Gamry Instruments). EIS was performed using a 50 mV AC amplitude from 100 kHz to 5 mHz at 0.2 V *vs.* Li/Li^+. These electrochemical characterizations were performed thrice on each electrode studied to verify repeatability of results observed.

Specific energy and power calculations

Specific energy was calculated by multiplying the first cycle specific discharge capacity (Ah kg_{Si}^{-1} or Ah kg_{total}^{-1} at that C-rate) by the potential window of silicon anode studied. Specific power was calculated by dividing specific energy with time required (in h) for lithiation of silicon. To calculate time required for lithiation, the specific discharge capacity was divided by the current density (in A kg^{-1}). It was noted that some reports consider silicon and the conductive matrix as the active material, but here we considered "only silicon" as the active material.

$$\text{Specific energy}(\text{Wh kg}^{-1}) = \text{Discharge capacity}(\text{Ah kg}^{-1}) \times \text{Potential window} \quad (1)$$

$$\text{Time for lithiation}(\text{h}) = \frac{\text{Disharge capacity}(\text{Ah kg}^{-1})}{\text{Current density}(\text{A kg}^{-1})} \quad (2)$$

$$\text{Specific power } (\text{W kg}_{\text{total}}^{-1}) = \frac{\text{Specific energy } (\text{Wh kg}^{-1})}{\text{Time for lithiation}(\text{h})} \quad (3)$$

Results and discussion

Composite binders were prepared from freeze-dried MXenes dispersed in a 1 wt% Alg solution in water by bath sonication (Fig. S3a†). Two composite binder compositions were investigated: 90 wt% Alg + 10 wt% MXenes and 80 wt% Alg + 20 wt% MXenes. These compositions were selected because they represented the minimal amount of MXene additives required to achieve reasonable electrochemical performance, shown below. The resulting Alg + MXene dispersions were stable and homogeneous, whereas a similar CB/Alg mixture did not disperse well, (Fig. S3a and b†). This result may be attributed to hydrogen bonding between –OH groups on the hydrophilic MXene nanosheet surface and the Alg. In contrast, CB does not possess hydrogen bonding groups and is hydrophobic.

To further analyze the composite binder, attenuated total reflection – Fourier transform infrared (ATR-FTIR) spectroscopy analysis was performed on drop-cast Alg, drop-cast MXene nanosheets, and the two drop-cast composite binders, Fig. 1e. The Alg FTIR spectrum demonstrated absorbance peaks at 3300 cm^{-1} (–OH stretching), 1600 cm^{-1} (O–C–O asymmetric vibration), 1420 cm^{-1} (O–C–O symmetric vibration), ~1300 cm^{-1} (deformation of pyranose rings), and 1020 cm^{-1} (C–O–C symmetric vibrations), consistent with literature.[20,43] The MXene FTIR spectrum demonstrated absorbance peaks at 1050 cm^{-1} (C–O), 1100 cm^{-1} (C–F), and 1395 cm^{-1} (O–H), which confirms the presence of terminal surface groups on MXenes, particularly hydroxyl groups.[44,45] The FTIR spectra of both Alg + MX composite binders demonstrated peaks from the constituent species as well as a slight reduction in the –OH stretching peak area, which might be attributed to hydrogen bonding between the two species.[46]

Silicon-based electrodes were fabricated from the two composite binders to create two electrodes bearing Si/Alg/MX mass compositions of 80/18/2 and 80/16/4. The former resulted from the 90 wt% Alg + 10 wt% MXenes composite binder, and the latter resulted from the 80 wt% Alg + 20 wt% MXene composite binder. In early screening experiments, we determined that the electrode with 4 wt% MXene nanosheets demonstrated higher capacities than the one with 2 wt% MXenes (Fig. S4†). This can be attributed to lower electronic conductivity of 90 wt% Alg + 10 wt% MXenes composite binder (1×10^{-6} S cm^{-1}) as compared to 80 wt% Alg + 20 wt% MXenes (2.62×10^{-4} S cm^{-1}). This shows that proper balance between binder and conductive additive is essential to obtain optimum cycling performance. With the purpose of this investigation being to minimize the MXene loading, we did not explore other compositions. Thus, all further experiments focused upon the Si/Alg/MX composition of 80/16/4 (by mass), for which the active material loading was 0.70 ± 0.05 mg cm^{-2}. Other mass loadings of 0.3 to 2.2 mg cm^{-2} are discussed in the ESI.†

To analyse the interactions between silicon nanoparticles, Alg binder, and MXene nanosheets, FTIR spectroscopy was performed (Fig. 1e). The FTIR spectrum of Si/Alg/MX contained peaks from each of the three materials. The –OH stretching peak around 3300 cm^{-1} can be attributed to hydrogen bonding interactions among the three species.[46]

The electrochemical performance of silicon electrodes was evaluated in lithium metal half-cells with 1 M $LiPF_6$ in EC : DEC with 10 wt% FEC as the electrolyte. The electrodes were first conditioned by three cycles of charge–discharge at 0.1 C to form an SEI (data not shown). Fig. 2 shows the subsequent cyclic voltammograms (CVs) (for the third cycle) of Si/Alg = 80/20, Si/Alg/CB = 80/16/4, and Si/Alg/MX = 80/16/4 electrodes at scan rate of 0.1 mV s^{-1}. The CV for Si/Alg shows a

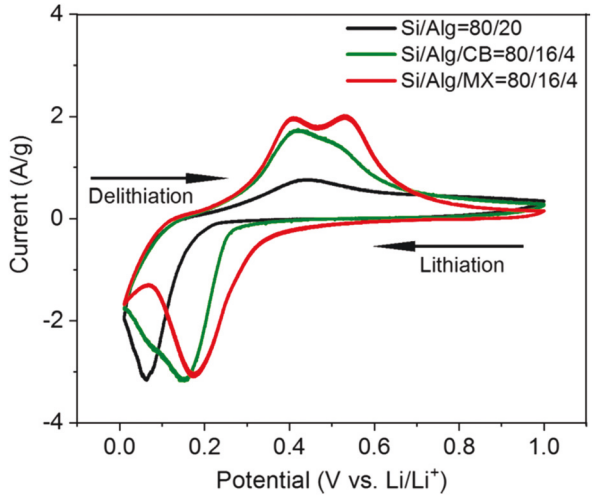

Fig. 2 Cyclic voltammograms of Si/Alg = 80/20, Si/Alg/CB = 80/16/4, and Si/Alg/MX = 80/16/4 at scan rate of 0.1 mV s^{-1}. Cyclic voltammetry was performed for five cycles at 0.1 mV s^{-1} and the third cycle for each is shown here. The current is normalized by mass of silicon. Before CV, conditioning was performed at 0.1 C for three cycles.

lithiation peak at 0.1 V and a broad delithiation peak at 0.4 V. Si/Alg also exhibited the lowest anodic current response compared to Si/Alg/CB and Si/Alg/MX, which we attribute to the sluggish kinetics and lower electrochemical activity caused by the absence of conductive additives. The CVs of Si/Alg/CB and Si/Alg/MX show distinct lithiation peaks at 0.2 V and two delithiation peaks at 0.4 and 0.6 V, which are consistent with those found in the literature.[47] Si/Alg/MX demonstrated highest anodic current response as compared to other two electrodes. Also, the potential difference between the lithiation and delithiation peaks for Si/Alg/MX was smaller than other two electrodes. This result indicates that MXene nanosheets provide a better formed electronic network in the electrode which lowers the degree of polarization.[37]

MXenes are electrochemically active in the potential window of 0 V to 3 V *vs.* Li/Li^+,[31,32,48] but no additional redox peaks were observed here for Si/Alg/MX. This absence is attributed to the low MXene concentration (4 wt% in the entire electrode), such that the dominating response was that of silicon.

Next, we evaluated the long-term cycling performance of Si/Alg, Si/Alg/CB, and Si/Alg/MX electrodes, in which the electrodes were cycled at 0.1 C (five times) and then at 0.5 C (195 times). Si/Alg/MX demonstrated the highest capacity throughout cycling, followed by Si/Alg/CB and Si/Alg (Fig. 3a). All electrodes exhibited a drop in capacity for the first few cycles due to the increase in C-rate and also due to the gradual build-up of the SEI.[49] Fig. S5† shows the galvanostatic response of the first cycle plot at 0.1 C; all three electrodes show a broad plateau at ~0.2 V *vs.* Li/Li^+ assigned to the conversion of crys-

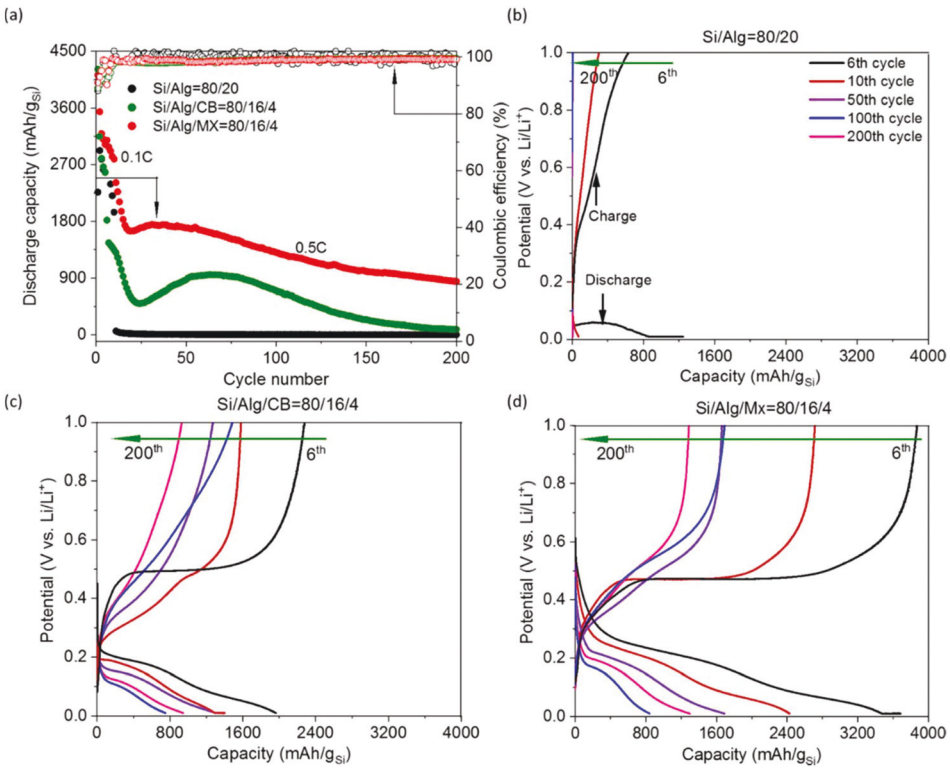

Fig. 3 (a) Comparison of cycling performance of Si/Alg = 80/20, Si/Alg/CB = 80/16/4, and Si/Alg/MX = 80/16/4 electrodes. Cycling was performed at 0.1 C for first 5 cycles in constant current-constant voltage mode followed by cycling at 0.5 C in constant current mode for the remaining cycles. Voltage profiles at the 6th, 10th, 50th, 100th, and 200th cycles (all at 0.5 C) for (b) Si/Alg = 80/20, (c) Si/Alg/CB = 80/16/4, and (d) Si/Alg/MX = 80/16/4 electrode. Voltage profile for first cycle at 0.1 C is shown in Fig. S5.† The active material loading was around 0.70 ± 0.05 mg cm^{-2}.

talline silicon to lithiated amorphous silicon.[1,50,51] Si/Alg, Si/Alg/CB, and Si/Alg/MX demonstrated initial capacities of 2170, 3320, 3800 mA h g_{Si}^{-1}, respectively. The initial coulombic efficiency (ICE) of Si/Alg/MX was the highest (~80%), followed by Si/Alg (~78%) and Si/Alg/CB (~64%). The very low ICE of Si/Alg/CB can be attributed to lithium trapping associated with the amorphous carbon.[39]

The effect of silicon mass loading and MXene oxidation on silicon anode performance are described separately (Fig. S7 and S8†). We observed that higher loadings (>0.7 mg cm^{-2}) showed poor adhesion to the current collector and that further optimization will be required to improve adhesion which is beyond the scope of our study.

The galvanostatic voltage responses for selected cycles (6^{th} to 100^{th}) are shown in Fig. 3b–d. Si/Alg showed a dramatic decrease in capacity after the first cycle (Fig. 3b) owing to delamination from the current collector after 200 cycles (Fig. S6†). Si/Alg/CB showed higher capacities than Si/Alg for 150 cycles (Fig. 3a and c) which then dropped to almost 50 mA h g_{Si}^{-1} at the end of 200 cycles. On the other hand, Si/Alg/MX showed the highest capacity and most consistent voltage profiles throughout the 200 cycles (Fig. 3a and d). The capacities can be further improved by pre-lithiation, tuning silicon particles, modifying MXene surface, modifying electrolyte, and so on which is beyond the scope of his study.

The superior cycling performance for Si/Alg/MX implies that 4 wt% MXenes is sufficient to sustain long term cycling without delamination (Fig. S6†). We attribute this result to hydrogen bonding interactions among –OH groups on the MXene nanosheet surface, the silicon surface, and Alg binder. The satisfactory capacity for Si/Alg/MX is further attributed to improved electrical connections afforded by the high aspect ratio MXene nanosheets. In contrast, the capacity of the Si/Alg/CB electrode was inferior, which we attribute to insufficient electrical connections because of possible aggregation of the hydrophobic CB particles. Overall, this highlights the importance of fabricating silicon anodes with hydrophilic additives, rather than hydrophobic ones, when water is the processing medium.

To further understand the improved performance of the Si/Alg/MX electrode, we measured the electronic conductivities of Alg/MX and Alg/CB polymer composites (without silicon nanoparticles), Table S1.† This approach isolates the contribution of the additives alone without interference from the silicon active material. The sample with 80 wt% Alg and 20 wt% MXene nanosheets showed a higher electronic conductivity (2.62×10^{-4} S cm^{-1}) as compared to the sample consisting of 80 wt% Alg and 20 wt% CB (1.82×10^{-4} S cm^{-1}). This result is attributed to the higher conductivity of MXenes (4600 S cm^{-1})[52] in contrast to CB (50–100 S cm^{-1}).[53] This also confirms our observation of higher capacities achieved for Si/Alg/MX as opposed to Si/Alg/CB (Fig. 3).

We next performed electrochemical impedance spectroscopy (EIS) on Si/Alg, Si/Alg/CB, and Si/Alg/MX electrodes before and after 10 and 50 cycles to monitor changes in impedance at 0.2 V. Fig. 4 shows Nyquist plots with depressed semi-

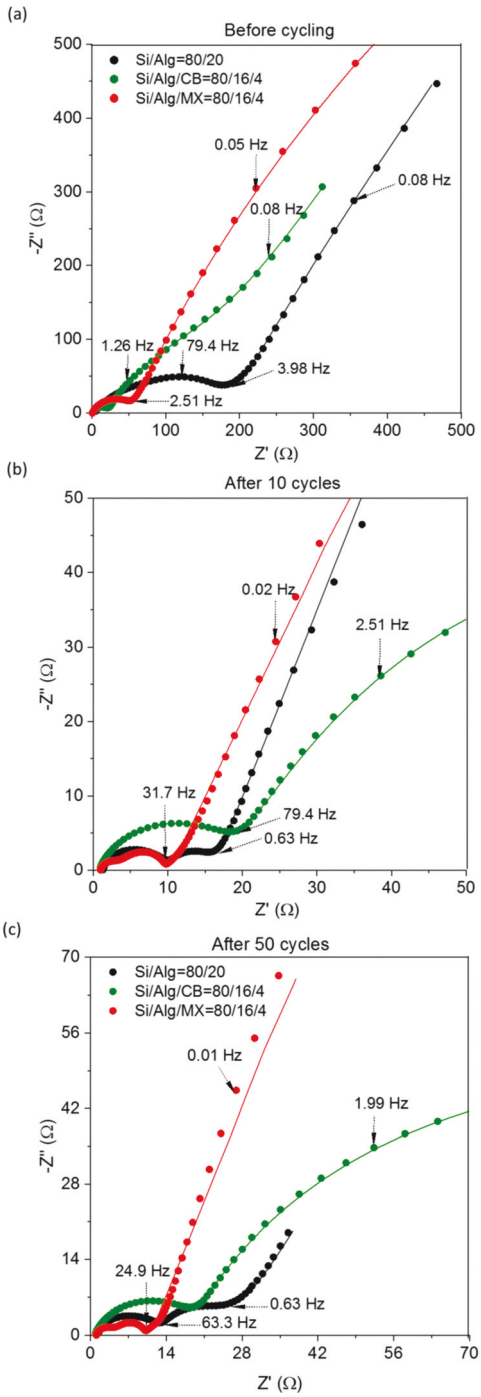

Fig. 4 Nyquist plot for (a) Si/Alg = 80/20, (b) Si/Alg/CB = 80/16/4, and (c) Si/Alg/MX = 80/16/4 electrode. Electrochemical impedance spectroscopy was performed with a frequency range from 100 kHz to 5 mHz with an amplitude of 10 mV around a potential of 0.2 V. The dotted lines represent the experimental data and solid lines represent the equivalent circuit model fit to the data, Fig. S9.†

circles in both the high and medium frequency regions and a Warburg tail in the low frequency region. For data before cycling (Fig. 4a), only one semi-circle was observed, which is indicative of a charge transfer resistance (R_{CT}). For data after cycling (Fig. 4b–c), two semicircles are observed; the one in the

high frequency region is attributed to SEI formation and the one in the medium frequency region is attributed to R_{CT}. To analyze the physical significance of electrochemical process occurring in these electrodes an equivalent circuit was employed. The circuit shown in Fig. S9a† was fit to the data before cycling, and the circuit shown in Fig. S9b† was fit to the data after cycling. The equivalent circuits consisted of an ohmic resistance (R_O), which is the resistance to Li^+ ion conduction through the bulk solution to the electrode–electrolyte interface and to the electronic conduction through the electrode to the copper foil-electrode interface; R_{CT} due to the reaction between the silicon and Li^+ ions; a constant phase element (CPE) due to the electrode–electrolyte interface; a resistance due to the SEI layer (R_{SEI}); a CPE due to the SEI layer-electrolyte interface; and a Warburg impedance (W_O) related to solid-state Li^+ ion diffusion.

Table S2† summarizes the equivalent circuit modelling. Si/Alg/MX demonstrated the lowest R_{CT} as compared to Si/Alg and Si/Alg/CB, both before and after cycling. All electrodes showed a drop in R_{CT} after cycling because of gradual electrolyte penetration.[54] After 10 cycles, the total resistance of Si/Alg/MX was 8.0 Ω and those for Si/Alg and Si/Alg/CB were 12.9 Ω and 28.6 Ω, respectively (Table S2†). After 50 cycles, all electrodes demonstrated an increase in resistance. However, the increase was more pronounced for Si/Alg (65%) and Si/Alg/CB (71%) as compared to Si/Alg/MX (48%). The solid-state diffusion coefficient of each electrode was calculated[55] using EIS and galvanostatic cycling results (see ESI and Fig. S10†). As seen in Table S2,† the Li^+ ion diffusion coefficient after 50 cycles of the Si/Alg/MX electrode (20.2×10^{-12} cm^2 s^{-1}) was much higher than that of Si/Alg and Si/Alg/CB electrodes.

The low R_{CT} and high Li^+ ion diffusion coefficient for Si/Alg/MX is a result of the higher conductivity of the electrode resulting from a better interconnected network due to MXene nanosheets. The high aspect ratio of the MXene nanosheets[13] allows for better connection between adjacent nanosheets even when only 4 wt% MXene nanosheets were used in the entire electrode. On the other hand, CB has a lower aspect ratio and thus lacks the ability to form a well-developed electronically connected path for such low concentrations. These properties ultimately led to improved performance of Si/Alg/MX over the control electrodes.

Typical scanning electron microscopy (SEM) images of Si/Alg, Si/Alg/CB and Si/Alg/MX electrodes before and after cycling are shown in Fig. 5. All electrodes before cycling have a very similar morphology. MXene nanosheets are visible at the Si/Alg/MX surface and in the cross-section, which was further confirmed by the presence of titanium (Ti) in the energy dispersive X-ray spectroscopy (EDS) images (Fig. S11†). After cycling, all electrodes exhibited an SEI layer; however, a more uniform SEI layer was formed on the Si/Alg/MX electrode, as opposed to patchy SEI formation on the other two electrodes. Although MXene nanosheets were not visible in the Si/Alg/MX SEM images after cycling because of the SEI layer, EDS images do show the presence of Ti throughout electrode (Fig. S11†).

We also performed X-ray photoelectron spectroscopy (XPS) on our electrodes before and after cycling. The XPS survey scan of Si/Alg/MX before cycling shows a Ti peak, in addition to Si,

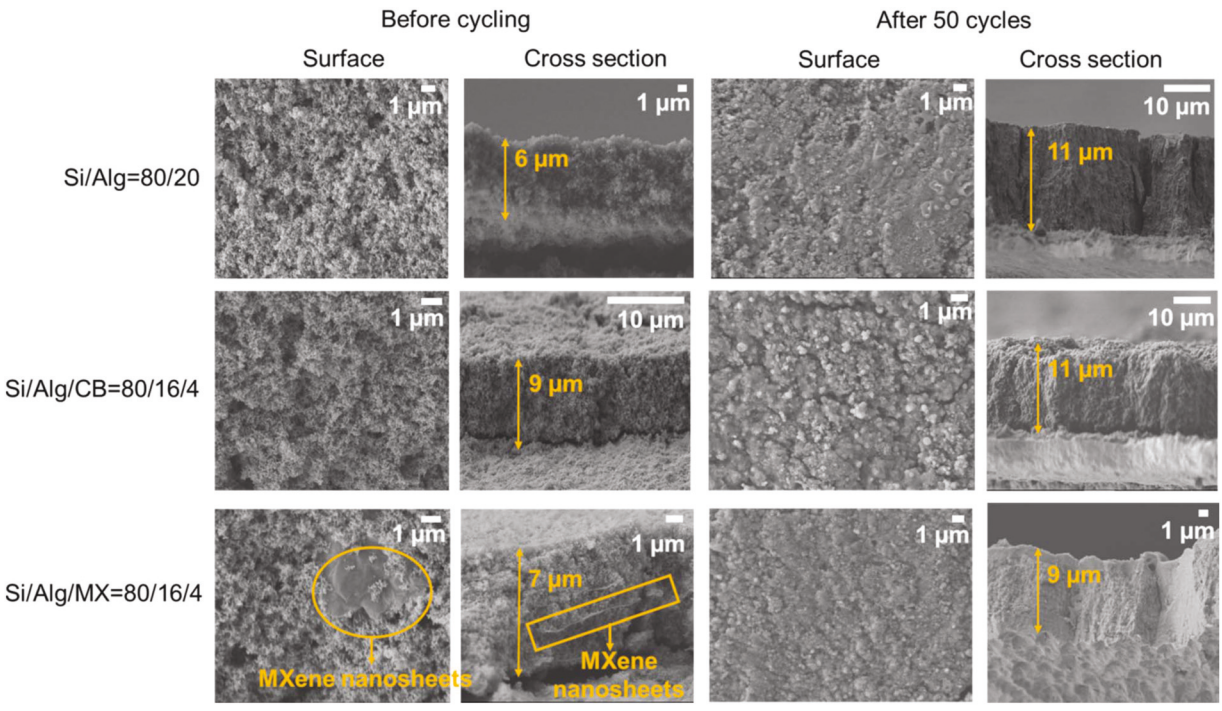

Fig. 5 Scanning electron microscopy (SEM) images (both surface and cross section) of Si/Alg = 80/20, Si/Alg/CB = 80/16/4, and Si/Alg/MX = 80/16/4 electrodes before and after 50 cycles.

C, O peaks observed in the other two electrodes (Fig. S12†). After cycling, XPS survey scans of all electrodes show fluorine (F) and lithium (Li) peaks, which are representative of an SEI layer (Fig. S12†). Typical SEI products for Si anodes[12,56–58] were observed in the deconvoluted peaks in Fig. S13–S15.† After cycling, the Ti peak for the Si/Alg/MX electrode was not observed in XPS survey scans, probably because it was buried under the SEI layer.

Fig. 6 shows the rate performance of the silicon electrodes at different C-rates ranging from 0.1 C to 5 C. The Si/Alg electrode exhibited the poorest rate performance, in which the capacity dropped to 10 mA h g_{Si}^{-1} at C-rates above 0.2 C. Comparing Si/Alg/CB and Si/Alg/MX electrodes, the latter showed higher capacities; specifically, the discharge capacity was 1050 mA h g_{Si}^{-1} at 1 C for Si/Alg/MX and 700 mA h g_{Si}^{-1} for Si/Alg/CB (Fig. S16†). All electrodes showed a drop in capacity with increase in C-rate due to diffusion limitation of Li^+ ions.[59] The capacity recovery (when C-rate was bought back to 0.1 C) of Si/Alg/MX was around 71%, as compared to 65% for Si/Alg/CB and 60% for Si/Alg. These results emphasize the improved rate capability and higher stability of Si/Alg/MX electrodes. The improved rate performance is also supported by our EIS results (Fig. 4, Table S2†), for which Si/Alg/MX electrodes exhibited the lowest R_{CT} and the highest Li^+ ion diffusion coefficient.

We constructed a Ragone plot (Fig. 7a) to compare the specific energy and power (normalized by total electrode mass) of our silicon electrodes to selected literature.[13,36,37,39,60–64] We first compare our results to silicon electrodes using reduced graphene oxide (rGO) nanosheets[61–63] or CNTs[39] as either conductive additives. The specific energy corresponding to the specific power of our silicon electrodes with only 4 wt% MXenes was comparable to those reported in literature with much higher rGO contents. However, there were a few exceptions: one reported by Chang *et al.* in which they made Si/rGO = 76/24 electrodes, other reported by Assresahegn *et al.* where they made 90 wt% PAA grafted silicon with 10 wt% rGO, and another reported by Wang *et al.* in which CNT-C microscrolls were added to achieve a very high silicon loading of 85 wt%.[39] To the best of our knowledge, there are no reports on silicon anodes with less than 10 wt% rGO as conductive additive probably because of poor dispersibility in water resulting in non-uniform electrode conductivity. Overall, this comparison implies that rGO nanosheets may be replaced with MXene nanosheets for silicon anodes in certain applications. The possible benefit is that MXenes are natively hydrophilic, making them ideal for water-based silicon anode processing. In contrast, rGO is hydrophobic and its formation requires a harsh reduction step.

Next, we compared our results to other reports that used MXenes in the silicon anode.[13,36,37,60] Within those, our electrodes – containing only 4 wt% MXene nanosheets – demonstrated the highest specific energies for the corresponding specific power on a total electrode mass basis. This is more clearly demonstrated in Fig. 7b, which displays a 3-D plot of specific energy, power density (both normalized by total electrode mass), and MXene content. The next-best-performing composition was 70 wt% silicon and 30 wt% MXenes, where no polymeric binder was required.[13] In contrast we required 16 wt% Alg binder because such a low MXene concentration (here, 4 wt%) was insufficient to act as a binder alone (Fig. S18†). Despite adding an insulating binder, our silicon electrodes exhibited superior results because of the high silicon content (80 wt%). Specifically, the Si/Alg/MX = 80/16/4 anode yielded the highest specific energy on a *total* electrode

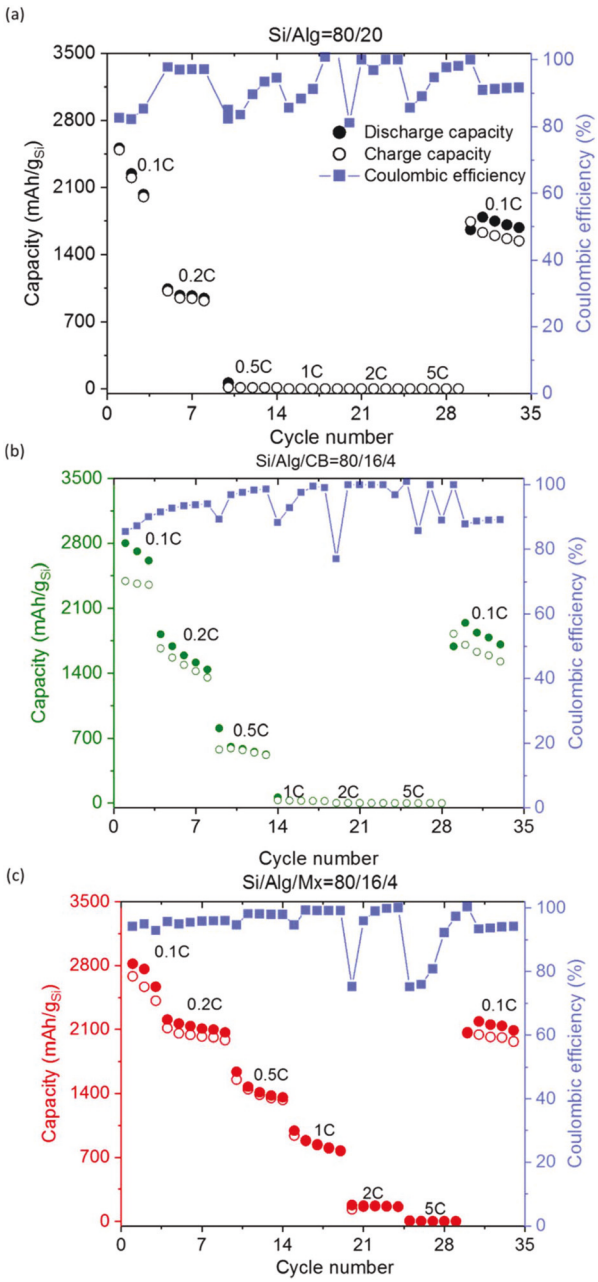

Fig. 6 Rate performance at different C-rates ranging from 0.1 C to 5 C for (a) Si/Alg = 80/20, (b) Si/Alg/CB = 80/16/4, (c) Si/Alg/MX = 80/16/4 electrode. The active material loading was around 0.70 ± 0.05 mg cm^{-2}. The C-rate was brought back to 0.1 C again to determine the capacity recovery.

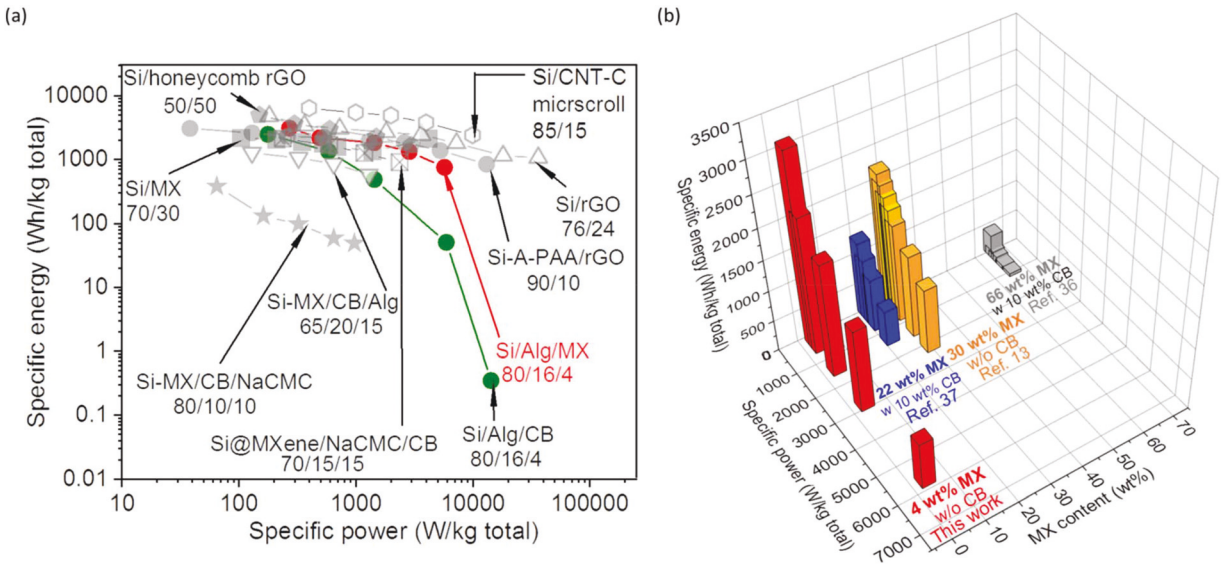

Fig. 7 (a) Ragone plot of specific energy *vs.* specific power (W kg^{-1}). (b) 3D plot with specific energy, specific power (both based on total electrode mass), and MXene content (wt%). Table S3† summarizes the data displayed here.

mass basis (3100 W h kg_{total}^{-1}) as comapred to other silicon-MXene constructs(~115–2000 W h kg_{total}^{-1}) at a corresponding specific power (~270 W kg_{total}^{-1}). Even lower specific energies were obtained by Zhu *et al.*[37] (22 wt% MXene) and Kong *et al.*[36] (66 wt% MXene) because those electrodes used only 44 wt% and 13 wt% silicon, respectively. These two reports also used hydrophobic carbon additives. Table S3† provides a summary of the data displayed in Fig. 7. From this comparison, we conclude that the large amounts of additives (>30 wt% MXenes, polymer, and/or carbon additive) lowered the active silicon content, which in turn reduced the total electrode's specific energy.

Conclusions

Here, we maximized silicon anode capacity by minimizing the amount of two-dimensional $Ti_3C_2T_x$ MXene nanosheet conductive additive. This was accomplished by replacing hydrophobic carbon additives with hydrophilic MXene additives, which facilitated water-based processing. We designed electrodes with a high silicon content of 80 wt%, 16 wt% Alg binder and 4 wt% MXene nanosheets. These electrodes demonstrated stable capacities around 900 mA h g_{Si}^{-1} (720 mA h g_{total}^{-1}) at a high C-rate of 0.5 C, which was higher than a comparable electrode made in-house containing 4 wt% carbon black. Despite having such a low MXene content (4 wt%), our electrodes exhibited specific energies comparable to electrode containing higher amounts of rGO or CNTs.[39,61–63]

The improved electrode performance is attributed to the enhanced conductivity owing to the large lateral MXene nanosheet size. The hydrophilic terminal groups on the MXene nanosheets allowed for slurry casting of homogeneous electrodes using water as the solvent, thus forming uniform electrical networks. Also, the possible hydrogen bonding interactions between hydroxyl groups of MXenes, Alg binder and silicon improved the overall electrode integrity. Thus, we show that the carbon additives can be eliminated and instead much lower content of MXenes can be used to create homogenous silicon electrodes. These electrodes showed high specific energies without compromising on the electrode integrity for 200 charge–discharge cycles. Our future work will be to further reduce the dead weight of the silicon electrode by utilizing different MXenes or by further lowering the binder content.

Conflicts of interest

There are no conflicts to declare.

Acknowledgements

This material is based upon work supported by National Science Foundation under grant no. 1760859 and National Research Foundation of Korea under grant no. NRF-2019R1A2C1004593. The authors thank the Material Characterization Facility at Texas A&M University, College Station. The authors also thank Tan Ngyuen and Laboratory for Synthetic-Biologic Interactions for assisting with Fourier transform infrared spectroscopy.

Notes and references

1 J.-Y. Li, Q. Xu, G. Li, Y.-X. Yin, L.-J. Wan and Y.-G. Guo, *Mater. Chem. Front.*, 2017, **1**, 1691–1708.

2 M. Li, J. Lu, Z. Chen and K. Amine, *Adv. Mater.*, 2018, **30**, 1–24.
3 X. Zuo, J. Zhu, P. Müller-Buschbaum and Y.-J. Cheng, *Nano Energy*, 2017, **31**, 113–143.
4 M. Salah, P. Murphy, C. Hall, C. Francis, R. Kerr and M. Fabretto, *J. Power Sources*, 2019, **414**, 48–67.
5 D. Ma, Z. Cao and A. Hu, *Nano-Micro Lett.*, 2014, **6**, 347–358.
6 A. F. Gonzalez, N. H. Yang and R. S. Liu, *J. Phys. Chem. C*, 2017, **121**, 27775–27787.
7 M. N. Obrovac and V. L. Chevrier, *Chem. Rev.*, 2014, **114**, 11444–11502.
8 S. Iwamura, H. Nishihara, Y. Ono, H. Morito, H. Yamane, H. Nara, T. Osaka and T. Kyotani, *Sci. Rep.*, 2015, **5**, 8085.
9 D. Liu, Z. J. Liu, X. Li, W. Xie, Q. Wang, Q. Liu, Y. Fu and D. He, *Small*, 2017, **13**, 1702000.
10 X. H. Liu, L. Zhong, S. Huang, S. X. Mao, T. Zhu and J. Y. Huang, *ACS Nano*, 2012, **6**, 1522–1531.
11 A. Wang, S. Kadam, H. Li, S. Shi and Y. Qi, *npj Comput. Mater.*, 2018, **4**, 15.
12 E. Peled and S. Menkin, *J. Electrochem. Soc.*, 2017, **164**, A1703–A1719.
13 C. Zhang, S.-H. Park, A. Seral-Ascaso, S. Barwich, N. McEvoy, C. S. Boland, J. N. Coleman, Y. Gogotsi and V. Nicolosi, *Nat. Commun.*, 2019, **10**, 849.
14 T. M. Higgins, S. H. Park, P. J. King, C. J. Zhang, N. McEvoy, N. C. Berner, D. Daly, A. Shmeliov, U. Khan, G. Duesberg, V. Nicolosi and J. N. Coleman, *ACS Nano*, 2016, **10**, 3702–3713.
15 T. W. Kwon, J. W. Choi and A. Coskun, *Chem. Soc. Rev.*, 2018, **47**, 2145–2164.
16 G. G. Eshetu and E. Figgemeier, *ChemSusChem*, 2019, **12**, 2515–2539.
17 A. Magasinski, B. Zdyrko, I. Kovalenko, B. Hertzberg, R. Burtovyy, C. F. Huebner, T. F. Fuller, I. Luzinov and G. Yushin, *ACS Appl. Mater. Interfaces*, 2010, **2**, 3004–3010.
18 W. Porcher, S. Chazelle, A. Boulineau, N. Mariage, J. P. Alper, T. Van Rompaey, J. -S. Bridel and C. Haon, *J. Electrochem. Soc.*, 2017, **164**, A3633–A3640.
19 C. C. Nguyen, T. Yoon, D. M. Seo, P. Guduru and B. L. Lucht, *ACS Appl. Mater. Interfaces*, 2016, **8**, 12211–12220.
20 I. Kovalenko, B. Zdyrko, A. Magasinski, B. Hertzberg, Z. Milicev, R. Burtovyy, I. Luzinov and G. Yushin, *Science*, 2011, **7**, 75–79.
21 Y. Bie, J. Yang, X. Liu, J. Wang, Y. Nuli and W. Lu, *ACS Appl. Mater. Interfaces*, 2016, **8**, 2899–2904.
22 D. N. Ho, O. Yildiz, P. Bradford, Y. Zhu and P. S. Fedkiw, *J. Appl. Electrochem.*, 2017, **48**, 127–133.
23 J. Luo, X. Zhao, J. Wu, H. D. Jang, H. H. Kung and J. Huang, *J. Phys. Chem. Lett.*, 2012, **3**, 1824–1829.
24 J. K. Lee, K. B. Smith, C. M. Hayner and H. H. Kung, *Chem. Commun.*, 2010, **46**, 2025–2027.
25 H. Tang, J. Zhang, Y. J. Zhang, Q. Q. Xiong, Y. Y. Tong, Y. Li, X. L. Wang, C. D. Gu and J. P. Tu, *J. Power Sources*, 2015, **286**, 431–437.
26 L.-F. Cui, L. Hu, J. W. Choi and Y. Cui, *ACS Nano*, 2010, **4**, 3671–3678.
27 W. Li, M. Li, J. A. Shi, X. Zhong, L. Gu and Y. Yu, *Nanoscale*, 2018, **10**, 12430–12435.
28 M. Naguib, V. N. Mochalin, M. W. Barsoum and Y. Gogotsi, *Adv. Mater.*, 2014, **26**, 992–1005.
29 L. Verger, V. Natu, M. Carey and M. W. Barsoum, *Trends Chem.*, 2019, **1**, 656–669.
30 X. Zhang, Z. Zhang and Z. Zhou, *J. Energy Chem.*, 2018, **27**, 73–85.
31 S. Sun, C. Liao, A. M. Hafez, H. Zhu and S. Wu, *Chem. Eng. J.*, 2018, **338**, 27–45.
32 S. J. Kim, M. Naguib, M. Zhao, C. Zhang, H.-T. Jung, M. W. Barsoum and Y. Gogotsi, *Electrochim. Acta*, 2015, **163**, 246–251.
33 Z. Ling, C. E. Ren, M. Q. Zhao, J. Yang, J. M. Giammarco, J. Qiu, M. W. Barsoum and Y. Gogotsi, *Proc. Natl. Acad. Sci. U. S. A., Early Ed.*, 2014, **111**, 16676–16681.
34 P. Sobolciak, A. Ali, M. K. Hassan, M. I. Helal, A. Tanvir, A. Popelka, M. A. Al-Maadeed, I. Krupa and K. A. Mahmoud, *PLoS One*, 2017, **12**, e0183705.
35 M. Naguib, T. Saito, S. Lai, M. S. Rager, T. Aytug, M. Parans Paranthaman, M.-Q. Zhao and Y. Gogotsi, *RSC Adv.*, 2016, **6**, 72069–72073.
36 F. Kong, X. He, Q. Liu, X. Qi, D. Sun, Y. Zheng, R. Wang and Y. Bai, *Electrochem. Commun.*, 2018, **97**, 16–21.
37 X. Zhu, J. Shen, X. Chen, Y. Li, W. Peng, G. Zhang, F. Zhang and X. Fan, *Chem. Eng. J.*, 2019, **378**, 122212.
38 W. Zeng, L. Wang, X. Peng, T. Liu, Y. Jiang, F. Qin, L. Hu, P. K. Chu, K. Huo and Y. Zhou, *Adv. Energy Mater.*, 2018, **8**, 1702314.
39 H. Wang, J. Fu, C. Wang, J. Wang, A. Yang, C. Li, Q. Sun, Y. Cui and H. Li, *Energy Environ. Sci.*, 2020, **13**, 848–858.
40 L. Wang, T. Liu, X. Peng, W. Zeng, Z. Jin, W. Tian, B. Gao, Y. Zhou, P. K. Chu and K. Huo, *Adv. Funct. Mater.*, 2018, **28**, 1704858–1704866.
41 M. K. Dufficy, S. A. Khan and P. S. Fedkiw, *J. Mater. Chem. A*, 2015, **3**, 12023–12030.
42 M. Alhabeb, K. Maleski, B. Anasori, P. Lelyukh, L. Clark, S. Sin and Y. Gogotsi, *Chem. Mater.*, 2017, **29**, 7633–7644.
43 T. A. Fenoradosoa, G. Ali, C. Delattre, C. Laroche, E. Petit, A. Wadouachi and P. Michaud, *J. Appl. Phycol.*, 2009, **22**, 131–137.
44 S. Xu, G. Wei, J. Li, Y. Ji, N. Klyui, V. Izotov and W. Han, *Chem. Eng. J.*, 2017, **317**, 1026–1036.
45 L. Wang, L. Chen, P. Song, C. Liang, Y. Lu, H. Qiu, Y. Zhang, J. Kong and J. Gu, *Composites, Part B*, 2019, **171**, 111–118.
46 X. Wu, L. Hao, J. Zhang, X. Zhang, J. Wang and J. Liu, *J. Membr. Sci.*, 2016, **515**, 175–188.
47 B. Jerliu, E. Huger, L. Dorrer, B. K. Seidlhofer, R. Steitz, M. Horisberger and H. Schmidt, *Phys. Chem. Chem. Phys.*, 2018, **20**, 23480–23491.
48 B.-M. Jun, S. Kim, J. Heo, C. M. Park, N. Her, M. Jang, Y. Huang, J. Han and Y. Yoon, *Nano Res.*, 2018, **12**, 471–487.

49 J. Lia and J. R. Dahn, *J. Electrochem. Soc.*, 2007, **154**, A156–A161.
50 H. Wu, G. Yu, L. Pan, N. Liu, M. T. McDowell, Z. Bao and Y. Cui, *Nat. Commun.*, 2013, **4**, 1943.
51 K. Feng, M. Li, W. Liu, A. G. Kashkooli, X. Xiao, M. Cai and Z. Chen, *Small*, 2018, **14**, 1702737.
52 C. Zhang, Y. Ma, X. Zhang, S. Abdolhosseinzadeh, H. Sheng, W. Lan, A. Pakdel, J. Heier and F. Nüesch, *Energy Environ. Mater.*, 2020, **3**, 29–55.
53 J. Sánchez-González, A. Macías-García, M. F. Alexandre-Franco and V. Gómez-Serrano, *Carbon*, 2005, **43**, 741–747.
54 Y. Zhao, L. Yang, Y. Zuo, Z. Song, F. Liu, K. Li and F. Pan, *ACS Appl. Mater. Interfaces*, 2018, **10**, 27795–27800.
55 J. Xie, N. Imanishi, T. Zhang, A. Hirano, Y. Takeda and O. Yamamoto, *Mater. Chem. Phys.*, 2010, **120**, 421–425.
56 Y. Xu, E. Swaans, S. Chen, S. Basak, P. P. R. M. L. Harks, B. Peng, H. W. Zandbergen, D. M. Borsa and F. M. Mulder, *Nano Energy*, 2017, **38**, 477–485.
57 E. Radvanyi, W. Porcher, E. De Vito, A. Montani, S. Franger and S. J. S. Larbi, *Phys. Chem. Chem. Phys.*, 2014, **16**, 17142–17153.
58 Q. Li, X. Liu, X. Han, Y. Xiang, G. Zhong, J. Wang, B. Zheng, J. Zhou and Y. Yang, *ACS Appl. Mater. Interfaces*, 2019, **11**, 14066–14075.
59 W. Luo, X. Chen, Y. Xia, M. Chen, L. Wang, Q. Wang, W. Li and J. Yang, *Adv. Energy Mater.*, 2017, **7**, 1701083.
60 Y. Tian, Y. An and J. Feng, *ACS Appl. Mater. Interfaces*, 2019, **11**, 10004–10011.
61 H. Tang, J.-P. Tu, X.-Y. Liu, Y.-J. Zhang, S. Huang, W.-Z. Li, X.-L. Wang and C.-D. Gu, *J. Mater. Chem. A*, 2014, **2**, 5834–5840.
62 B. D. Assresahegn, B. D. Ossonon and D. Bélanger, *J. Power Sources*, 2018, **391**, 41–50.
63 J. Chang, X. Huang, G. Zhou, S. Cui, P. B. Hallac, J. Jiang, P. T. Hurley and J. Chen, *Adv. Mater.*, 2014, **26**, 758–764.
64 Y. Yan, X. Zhao, H. Dou, J. Wei, Z. Sun, Y. S. He, Q. Dong, H. Xu and X. Yang, *ACS Appl. Mater. Interfaces*, 2020, **12**, 18541–18550.